**ATLAS CONF Note**

ATLAS-CONF-2019-004

18th March 2019

# Measurement of Higgs boson production in association with a $t\bar{t}$ pair in the diphoton decay channel using 139 fb$^{-1}$ of LHC data collected at $\sqrt{s}$ = 13 TeV by the ATLAS experiment

## The ATLAS Collaboration

The measurement of Higgs boson production in association with a top quark-antiquark pair in the diphoton decay channel ($H \rightarrow \gamma\gamma$) is presented, based on the analysis of 139 fb$^{-1}$ of proton-proton collision data with center-of-mass energy $\sqrt{s}$ = 13 TeV recorded with the ATLAS detector at the Large Hadron Collider. The analysis is performed using a simultaneous fit in seven signal-enriched event categories. The $t\bar{t}H$ process is observed in the diphoton decay mode with a significance of 4.9 standard deviations relative to the background-only hypothesis. The expected significance is 4.2 standard deviations. The $t\bar{t}H$ cross-section times the $H \rightarrow \gamma\gamma$ branching ratio is measured to be $\sigma_{t\bar{t}H} \times B_{\gamma\gamma} = 1.59^{+0.43}_{-0.39}$ fb, in agreement with the Standard Model prediction.

# 1 Introduction

Since its discovery by the ATLAS and CMS Collaborations [1, 2], the Higgs boson and its interactions with other fundamental particles have been studied in great detail. Of particular interest is its coupling to the top quark, the heaviest particle in the SM. The strength of this interaction can be studied through the analysis of top-associated Higgs production ($t\bar{t}H$) events, which provides a tree-level probe of the top Yukawa coupling. This process was observed by both the ATLAS and CMS Collaborations in 2018 [3, 4] through the combination of several decay channels.

This note presents the results of the ATLAS search for $t\bar{t}H$ production in the $H \rightarrow \gamma\gamma$ decay channel using the full Run 2 (2015–2018) proton-proton collision data set with center-of-mass energy $\sqrt{s}$ = 13 TeV, corresponding to 139 fb$^{-1}$. The analysis utilizes the same event selection and categorization as that of the previous analysis [3] (based on 79.8 fb$^{-1}$ of Run 2 data), but with updated photon identification and jet calibration.

# 2 ATLAS detector

The ATLAS detector [5] is a multi-purpose particle detector with a forward-backward symmetric cylindrical geometry and almost $4\pi$ coverage in solid angle[1]. The inner tracking detector (ID) [6] covers $|\eta| < 2.5$ in pseudorapidity and consists of a silicon pixel detector, a silicon microstrip detector, and a transition radiation tracker. The ID is surrounded by a superconducting solenoid and a hermetic calorimeter system, which provides three-dimensional reconstruction of particle showers up to $|\eta| = 4.9$. The electromagnetic (EM) calorimeter is a lead/liquid-argon (LAr) sampling calorimeter, measuring electromagnetic showers in the barrel ($|\eta| < 1.475$) and endcap ($1.375 < |\eta| < 3.2$) regions. The hadronic calorimeter reconstructs hadronic showers using steel and scintillator tiles ($|\eta| < 1.7$), copper/LAr ($1.5 < |\eta| < 3.2$), or copper–tungsten/LAr ($3.1 < |\eta| < 4.9$). A muon spectrometer (MS) surrounds the calorimeter system. It comprises separate trigger chambers ($|\eta| < 2.4$) and precision tracking chambers ($|\eta| < 2.7$), in a magnetic field provided by three superconducting air-core toroids.

ATLAS data-taking uses a two-level trigger system [7]: a hardware-based first-level (L1) trigger component, reducing the event rate to at most 100 kHz, and a software-based high-level trigger component, reducing the event rate to approximately 1 kHz.

# 3 Data Set

The data set utilized includes the full Run 2 proton-proton collision data with center-of-mass energy $\sqrt{s}$ = 13 TeV recorded by the ATLAS detector between 2015 and 2018. The data set amounts to an integrated luminosity of 139±2 fb$^{-1}$ once data quality requirements (in order to ensure all detector components are operational) are imposed. The mean number of interactions $\langle\mu\rangle$ for the data set is 34 per bunch crossing. For the 2015–2016 data taking period, the average $\mu$ per bunch crossing was 23, while for

---

[1] ATLAS uses a right-handed coordinate system with its origin at the nominal interaction point (IP) in the centre of the detector and the $z$-axis along the beam pipe. The $x$-axis points from the IP to the centre of the LHC ring, and the $y$-axis points upward. Cylindrical coordinates $(r, \phi)$ are used in the transverse plane, $\phi$ being the azimuthal angle around the $z$-axis. The pseudorapidity is defined in terms of the polar angle $\theta$ as $\eta = -\ln\tan(\theta/2)$.

the 2017–2018 data taking period, it increased to 37. The trigger imposed in the 2015–2016 data taking period requires two photons with a *loose* online identification requirement, based on the energy leakage in the hadronic calorimeter and on the shower shape in the second layer of the EM calorimeter, and transverse energies of at least 25 and 35 GeV for the subleading and leading photons, respectively. Due to the increase of overlapping $pp$ collisions (pileup) and greater instantaneous luminosity in the 2017–2018 data taking period, the photon trigger identification requirement was tightened over that of the previous period to a *medium* selection, based on the energy leakage in the hadronic calorimeter and on the shower shape in the first and second layers of the EM calorimeter. Once the full diphoton event selection is applied (as described in Section 5), the average trigger efficiency for the 2015–2016 data taking period is found to be greater than 99% and, for the 2017–2018 data taking period, greater than 98%.

# 4 Event Simulation

The analysis uses Monte Carlo $t\bar{t}H$ signal events generated with the PoWHEG generator [8–11], with the PDF4LHC15 PDF set [12], and paired with PYTHIA8 [13] for parton showering and hadronization. The A14 set of parameters [14], tuned to data, are used here. The $b$-quark associated Higgs boson production mode ($b\bar{b}H$) is also generated with the PoWHEG generator and interfaced with PYTHIA8 using the A14 set of parameters.

Additional samples with other Higgs boson production modes, such as gluon-gluon fusion ($ggF$) [15], vector boson fusion ($VBF$) [16], and vector boson associated production ($VH$) [17, 18] are produced using the same generator and parton showering as for the $t\bar{t}H$ sample, but using the AZNLO set of parameters [19]. Samples with a Higgs boson produced in association with a single top-quark, including the $tHq$ and $tHW$ processes, are generated with the MADGRAPH5_aMC@NLO generator [20] using the CT10 PDF set [21]. PYTHIA8 is used for parton showering of the $tHq$ sample, with the A14 parameter set [14]. For the $tHW$ sample, parton showering is performed using HERWIG++ [22–24] with the UEEE5 parameter set. The simulated Higgs boson samples are normalized to their expected SM cross sections (as reported in Refs. [25–43]) times the expected SM branching ratio to diphotons (as reported in Refs. [25, 44–48]) at a center-of-mass energy of 13 TeV and with a Higgs boson mass of 125.09 GeV.

Although the analysis relies on data-driven background estimations, simulated background samples from the $t\bar{t}\gamma\gamma$ and continuum diphoton processes are generated in order to aid in choosing an analytic background function (as described in Section 6) and optimize the event selection. The $t\bar{t}\gamma\gamma$ events are generated using the MADGRAPH5_aMCNLO generator, showered with PYTHIA8 using both the PDF4LHC15 PDF set and the A14 parameter set. Continuum diphoton events are produced using the SHERPA 2.2.4 generator [49]. Next-to-leading-order matrix elements for diphotons plus zero or one jets and leading-order matrix elements for two or three jets are merged according to the ME+PS@NLO prescription [50] and using the CT10 PDF set and a dedicated parton shower tune [49].

All generated Higgs boson events are passed through a full simulation of the ATLAS detector response using GEANT4 [51]. The background samples (continuum diphoton and $t\bar{t}\gamma\gamma$ events) are processed with a fast simulation [52] in which the full simulation of the calorimeter is replaced with a parameterization of the calorimeter response [53]. The generation of the simulated event samples includes the effect of multiple $pp$ interactions per bunch crossing, as well as the effect on the detector response due to interactions from bunch crossings before or after the one containing the hard interaction. The simulated efficiency of passing the diphoton trigger is also corrected to match the measured trigger efficiency of the data.

# 5 Selection and Reconstruction

## 5.1 Photon Reconstruction and Identification

The photon identification and efficiency measurements, as well as energy calibration, have been updated since the analysis presented in Ref. [3]. Photon candidates are reconstructed from topological clusters [54] in the EM calorimeter [55, 56] and classified based upon cut-based identification requirements imposed on the electromagnetic calorimeter shower shape variables. Based on the levels of signal acceptance and background rejection of these cuts, two photon identification working points, *loose* and *tight*, are used. The loose selection is based on shower shapes in the second layer of the electromagnetic calorimeter and on the energy deposited in the hadronic calorimeter. The tight selections add information from the finely segmented strip layer of the calorimeter, and are separately optimized for unconverted and converted photons, to account for the generally broader lateral shower profile of the latter. However, the *tight* identification cut requirement is now optimized in sub-ranges of photon's transverse momentum ($p_T$), as the photon's electromagnetic shower depends significantly on its energy. Using the $p_T$-dependent *tight* photon identification cuts, photons with $p_T > 25$ GeV are expected to have a reconstruction and identification efficiency of greater than 82%. Compared to the previous analysis, the new selection provides an increase in fake photon rejection, while keeping the same identification efficiency.

After passing the diphoton trigger requirement described in Section 3, events are required to have at least two photons satisfying the offline *loose* identification requirement. Of the identified loose photon candidates, the two with the greatest $p_T$ are selected as the potential decay products of the Higgs boson. The information of the two *loose* photon candidates and the reconstructed vertices of the event are then fed into a neural network [57]. The neural network is trained using simulated $ggF$ ($H \rightarrow \gamma\gamma$) events to choose the vertex corresponding to the hard scatter event in which the Higgs boson is produced. When tested using simulated $t\bar{t}H$ signal events, it selects a vertex within 0.3mm of the correct vertex with a success rate of over 98%.

In addition to identification requirements on the photon EM calorimeter showers, isolation requirements are imposed on photon candidates in order to suppress jets misidentified as photons. The isolation requirement can be broken into two parts: the first part is a condition on the EM calorimeter information and the second part is a condition on information from the inner tracker. The EM calorimeter condition demands that the transverse energy deposited in clusters within a cone of $\Delta R < 0.2$ (with $\Delta R$ defined as $\sqrt{\Delta\phi^2 + \Delta\eta^2}$) surrounding the photon candidate in the EM calorimeter does not exceed 6.5% of the photon's transverse energy. Note that the deposited transverse energy is corrected for the average pileup transverse energy, and the transverse energy from the photon candidate is subtracted. The tracking-related condition demands that the scalar sum of the transverse momenta of tracks within a cone of $\Delta R < 0.2$ surrounding the photon be less than 5% of the photon candidate's $p_T$. Note that only tracks with $p_T > 1$ GeV and consistent with the reconstructed primary vertex[2] are considered. The isolation selection and methodology used is unchanged from that presented in Ref. [3]; however, updated systematic uncertainties associated with isolation efficiency have been implemented.

After the primary diphoton vertex has been determined, the photons are required to pass both the *tight* identification requirement and the isolation requirements. The two photons must also fall within the range of $|\eta| < 2.37$, as well as fall outside of the transition region between the central and endcap EM calorimeters,

---

[2] Studies of data sideband and simulated signal events have confirmed that the vertex chosen by the neural network and the primary vertex reconstructed from primary tracks are the same for greater than 99% of the events passing the $t\bar{t}H$ selection.

$1.37 < |\eta| < 1.52$. Kinematic cuts are imposed such that the $p_{\mathrm{T}}$ of the (sub)leading photon is $>0.35$ (0.25) times the the diphoton invariant mass, $m_{\gamma\gamma}$. Lastly, the diphoton invariant mass is required to fall within a window of $105 < m_{\gamma\gamma} < 160$ GeV. Events which satisfy these criteria (two *tight*-identified, isolated photons with satisfactory kinematic properties) are delineated as those passing the so-called *diphoton selection*.

## 5.2 Jet, Lepton, and Missing Transverse Momentum Reconstruction

Jet constituents are reconstructed from deposits of energy in the electromagnetic and hadronic calorimeters [54]. The anti-$k_t$ algorithm [58] is used to cluster jet constituents, using a radius parameter of 0.4. Reconstructed jets are required to have a transverse momentum $p_{\mathrm{T}} > 25$ GeV and a pseudorapidity $|\eta| < 4.4$. Of these jets, those with $|\eta| < 2.5$ and containing $b$-hadrons are identified using the MV2c10 $b$-tagging algorithm [59, 60] with the $b$-tagging average efficiency of 77%, corresponding to a light flavor mistagging rate of approximately 1%. In addition, jets with $p_{\mathrm{T}} < 120$ GeV and $|\eta| < 2.4$ which originate from pileup collisions are identified and removed via a jet vertex tagger multivariate discriminant [61].

Electrons and muons are reconstructed from tracks within the inner detector along with energy deposits in the electromagnetic calorimeter or tracks in the muon spectrometer, respectively. For electrons, energy deposits in the EM calorimeter are reconstructed identically to those from photons [56, 62]. The EM calorimeter information is combined with the matched tracking information from the ID and supplied to a likelihood discriminant in order to identify real electron candidates. The *Medium LH* identification requirement (as outlined in Ref. [62]) is used. Electron candidates in the analysis are required to have $p_{\mathrm{T}} > 15$ GeV and fall within the region of $|\eta| < 2.47$ (as well as fall outside of the transition region between the central and endcap EM calorimeters), and have $|z_0 \sin\theta| < 0.5$ mm (where $z_0$ is the longitudinal impact parameter along the beamline) in order to ensure consistency with the diphoton vertex. The electron candidate's transverse impact parameter $d_0$ (the transverse distance from the beamline) divided by its uncertainty $\sigma_{d_0}$ must be less than 5, also to ensure track and diphoton vertex compatibility. As with photons, isolation criteria derived from track and calorimeter information are applied to electron candidates in order to reject fake electron candidates. The *Fix (Loose)* (as outlined in Ref. [62]) criteria is chosen, for which the efficiency of real electrons considered in the analysis is greater than 95% for the range of $p_{\mathrm{T}} > 15$ GeV and $|\eta| < 2.47$.

Muon candidates in the analysis are required to have both $p_{\mathrm{T}} > 15$ GeV and $|\eta| < 2.7$. In addition, an identification requirement with the *medium* defined working point [63] is used to select real muons. As with electrons, additional constraints on the longitudinal and transverse impact parameters ($|z_0 \sin\theta| < 0.5$ mm and $|d_0|/\sigma_{d_0} < 3$) are imposed in order to ensure consistency between the muon candidate's track and the reconstructed diphoton vertex. Also as with electrons, isolation criteria derived from track and calorimeter information are imposed. These criteria were chosen such that the efficiency of real muons is greater than 95% for the range of $p_{\mathrm{T}} > 15$ GeV and $|\eta| < 2.7$.

The missing transverse momentum, $E_{\mathrm{T}}^{\mathrm{miss}}$, is defined as the negative vector sum of the transverse momenta of all objects associated with the reconstructed primary diphoton vertex. This includes photons, electrons, muons, jets, and any additional unidentified low-$p_{\mathrm{T}}$ tracks [64].

In order to remove double-counted objects, overlap removal criteria based on the distance apart $\Delta R$ of two objects in the detector is utilized, with cuts applied in the following sequence. First, electrons and jets overlapping ($\Delta R < 0.4$) with the two selected photons are removed. Second, jets overlapping ($\Delta R < 0.2$) with the remaining electrons are removed. Third, electrons overlapping ($\Delta R < 0.4$) with the remaining jets

are removed. Fourth, muons overlapping ($\Delta R < 0.4$) with the two selected photons are removed. Lastly, muons overlapping ($\Delta R < 0.4$) with the remaining jets are removed.

## 5.3 $t\bar{t}H$ Selection

In order to enhance the signal purity, an additional $t\bar{t}H$ *selection* is imposed in conjuntion with the diphoton selection. This $t\bar{t}H$ selection is unchanged with respect to that described in Ref. [3].

Events passing the diphoton selection and data quality requirements are further sorted into two $t\bar{t}H$-enriched regions. The "Lep" region, targeting $t\bar{t}$ decays in which at least one of the $W$ bosons decays to a muon or electron, requires events to have at least one isolated lepton (defined as a muon or electron) and at least one jet with $p_T > 25$ GeV and tagged as containing a $b$-hadron. The "Had" region targets hadronic top decays (as well as top decays to both hadronically-decaying $\tau$ leptons and unreconstructed leptons) and requires events to have at least one jet with $p_T > 25$ GeV and tagged as containing a $b$-hadron, as well as contain at least two additional jets with $p_T > 25$ GeV and no reconstructed leptons.

After events have been sorted into the $t\bar{t}H$-enriched regions, they are passed to a boosted decision tree (BDT) dedicated to either the respective "Lep" or "Had" selection. The BDTs are trained with the XGBoost package [65] to create regions of high $t\bar{t}H$ signal purity.

Both BDTs are trained using the transverse momentum $p_T$, the pseudorapidity $\eta$, and the azimuthal angle $\phi$ of the two photons in the event. In order to remove dependence on the invariant mass $m_{\gamma\gamma}$, the $p_T$ of the photons is divided by $m_{\gamma\gamma}$. The dedicated "Lep" BDT is also trained on: the $p_T$, $E$, $\eta$, and $\phi$ of up to two leptons; the $p_T$, $E$, $\eta$, and $\phi$ of up to four jets; and the magnitude and $\phi$ of the missing transverse energy $E_T^{\mathrm{miss}}$. Both the leptons and jets are passed in decreasing order of $p_T$. The dedicated "Had" BDT is trained on the $p_T$, $E$, $\eta$, $\phi$ and $b$-tag status of up to six jets and the magnitude and azimuthal angle of the $E_T^{\mathrm{miss}}$. Again, jets are passed in decreasing order of $p_T$. The BDTs were confirmed to be insensitive to the jet mass.

The "Lep" BDT is trained using 60% of the available $t\bar{t}H$ Monte Carlo events as a signal sample. Data events in which one or both of the photon candidates fail the isolation and/or identification requirement (defined as "not Tight/Isolated" events) are used as a background training sample. In addition, the $b$-tagged jet requirement from the "Lep" $t\bar{t}H$-enriched region selection is inverted, in order to increase training statistics. The leading jet in these events are labeled artificially as being $b$-tagged. The "Lep" BDT background training sample consists of 75% of these "not Tight/Isolated" events with no $b$-tagged jet. In order to increase background training statistics, the kinematic requirements on the leading and subleading photon candidates are loosened from $p_T/m_{\gamma\gamma} > 0.35$ and $p_T/m_{\gamma\gamma} > 0.25$ to $p_T > 35$ GeV and $p_T > 25$ GeV, respectively, and the diphoton invariant mass window is loosened from $105 < m_{\gamma\gamma} < 160$ GeV to $80 < m_{\gamma\gamma} < 250$ GeV. For consistency, the kinematic and diphoton invariant mass window requirements are loosened on the signal training sample, as well.

In addition to BDT training, subsets of both the signal and background samples are set aside for the purposes of: optimizing the BDT hyper-parameters, determining an optimal categorization based on BDT score, and testing against overtraining of the BDT. The "Lep" category uses 20% of the signal sample events for both hyper-parameter optimization and defining the BDT categories, and the final 20% for testing against overtraining of the BDT. As far as the background sample is concerned, the remaining 25% of the 0 $b$-tagged jet, "not Tight/Isolated" sample is used for hyper-parameter optimization. The "not Tight/Isolated" events *with* a $b$-tagged jet are used for the remaining tasks: 50% for optimally defining the BDT categories

(a) "Had" Region BDT Score Distributions
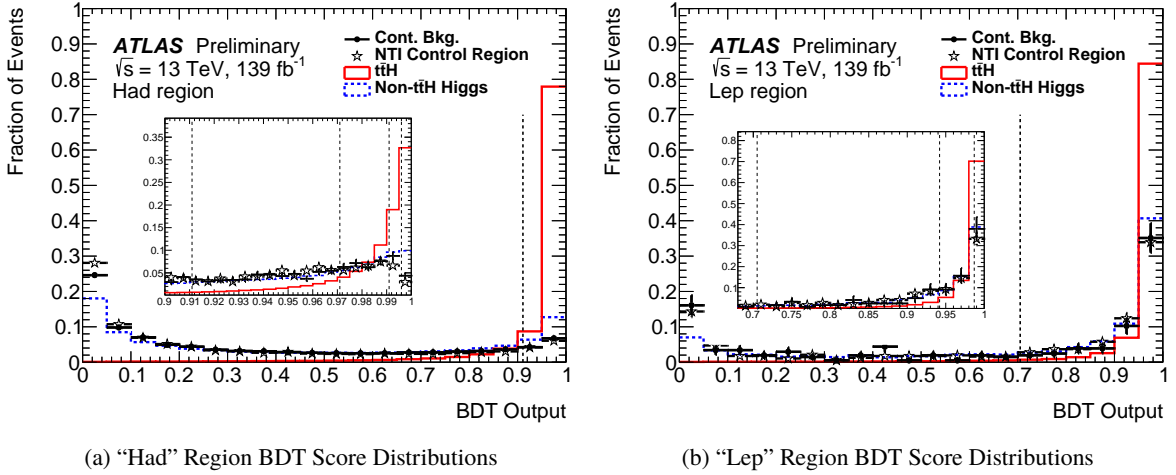
(b) "Lep" Region BDT Score Distributions

Figure 1: The normalized fraction of events in bins of BDT score in the (a) "Had" and (b) "Lep" regions of: simulated $t\bar{t}H$ signal events (red); simulated non-$t\bar{t}H$ Higgs boson events (blue); "Not Tight/Isolated" (NTI) data events used as the background sample in testing the BDTs (open stars); and data sideband events (filled black circles). The "Not Tight/Isolated" data events shown are those used in testing the BDTs, and, as such, they are required to pass all cuts in the diphoton and $t\bar{t}H$ preselections, other than the identification and isolation criteria. The dashed lines on the $x$-axis denote the BDT-score cut of the loosest category in each region. The insets provide a zoomed-in picture of the BDT score distribution for events which are selected for the BDT categories. The dashed lines in the insets denote the category boundaries.

and 50% for testing. As with the training samples, the requirements on the leading and subleading photon kinematics and the diphoton invariant mass are loosened in both the signal and background samples, in order to increase the background statistics available for hyper-parameter optimization.

As with the "Lep" BDT, the "Had" BDT is trained using 60% of the available $t\bar{t}H$ Monte Carlo events as a signal sample. The "Had" region BDT also utilizes "not Tight/Isolated" events as a background sample, with 60% of these events in the "Had" $t\bar{t}H$-enriched region used for BDT training. Aside from training, 20% of the signal and background samples are used for both hyper-parameter optimization and categorization. The final 20% of the signal and background samples is used for testing. Unlike with the "Lep" BDT, the photon kinematic and diphoton invariant mass requirements, as well as the $b$-tagged jet requirement, are not loosened for the training or hyper-parameter optimization.

Finally, events in the $t\bar{t}H$-enriched "Had" and "Lep" pre-selection regions are sorted into one of four "Had" or three "Lep" categories based on BDT score. The categories are labeled by their type ("Had" or "Lep") and by a number. The numbering scheme is chosen such that the category with the highest signal purity in each of the "Had" and "Lep" regions is labeled as category 1, while that with the lowest signal purity is labeled with the largest number. The distributions of $t\bar{t}H$ signal MC events and background events as a function of BDT score are presented in Figure 1. The figure presents the distributions for both the background samples used for the BDT training and the background events from the data sidebands (events which fall in the invariant mass window of $105 < m_{\gamma\gamma} < 120$ or $130 < m_{\gamma\gamma} < 160$ GeV). Good agreement in BDT response is observed, confirming that the training sample based on loosened-selection criteria does correctly reproduce the features of the background passing through the nominal analysis selection.
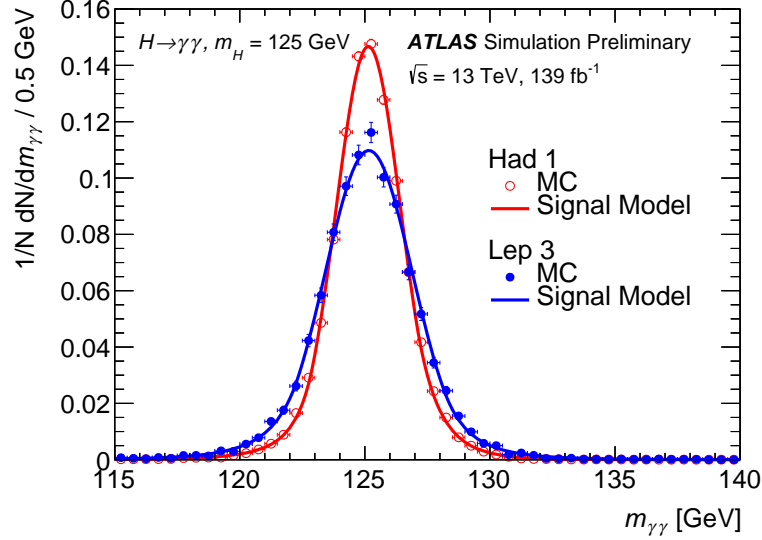
Figure 2: Examples of Higgs boson $m_{\gamma\gamma}$ signal shapes parameterized with a Double Sided Crystal Ball (DSCB) function for both the category with the best resolution ("Had" category 1) in red and the category with the worst resolution ("Lep" category 3) in blue. The resolution, defined as the width in GeV of the smallest window containing 90% ($\sigma_{90}$) of the inclusive Higgs boson signal events, of the "Had 1" category is $\sigma_{90}$ = 2.48 GeV, while that of the "Lep 3" category is $\sigma_{90}$ = 3.30 GeV. The open red and closed blue circles mark the simulated invariant mass distribution in "Had" category 1 and "Lep" category 3, respectively. The red and blue lines show the DSCB fits to the simulated distributions in "Had" category 1 and "Lep" category 3, respectively.

# 6 Signal and Background Modeling

For each of the $t\bar{t}H$-enriched BDT categories, the expected yield of Higgs boson events from all production modes (including, but not limited to, $t\bar{t}H$) is calculated using the simulated Higgs signal samples described in Section 4. The inclusive Higgs boson signal shape is modeled analytically using a double-sided Crystal Ball (DSCB) function [66, 67], which models the central portion of the signal as a Gaussian peak and the outer tails of the signal as power-law curves. Examples of fitted Higgs boson signals in two of the $t\bar{t}H$-enriched BDT categories are presented in Figure 2. The Higgs boson signal resolution in each category is presented in Table 1. The improvement in signal resolution observed in the purest BDT categories is due to the BDT preferentially selecting central Higgs boson events with higher $p_T$.

The shape of the background diphoton events is modeled with either a power law function or an exponential function. Note that only one-parameter (aside from normalization) functions are chosen due to the low statistics available in the data. In order to decide between the two functional forms, as well as confirm that the residual bias from the chosen functional form is small, a *spurious signal* test (as detailed in Ref. [1]) is used to determine which function agrees best with the predicted background shape, taken from a specified background-only sample. The continuum diphoton samples were found to have insufficient statistics in order to serve as background-only samples in the test. For the "Had" $t\bar{t}H$ categories, the background-only sample is defined as the "not Tight/Isolated" events containing at least three jets with $p_T$ > 25 GeV and no leptons. This selection is similar to the $t\bar{t}H$ "Had" preselection, except for the $b$-tagged jet requirement, which is removed in order to gain more statistics and hence obtain a smoother background shape. For the "Lep"categories, both "Tight/Isolated" and "not Tight/Isolated" simulated $t\bar{t}\gamma\gamma$ events are used. In

Table 1: The Higgs boson signal resolution, defined as the width in GeV of the smallest window containing 68% ($\sigma_{68}$) and 90% ($\sigma_{90}$) of the inclusive Higgs boson signal events , in each of the $t\bar{t}H$-enriched BDT categories. The categories are ordered such that the category with the highest signal purity in each of the "Had" and "Lep" regions is labeled as category 1, while that with the lowest signal purity is labeled with the largest number. Note that these are the expected values extracted from the MC samples at $m_H$ = 125 GeV.

| Category | $\sigma_{68}$ (GeV) | $\sigma_{90}$ (GeV) |
|---|---|---|
| "Lep" Category 1 | 1.56 | 2.80 |
| "Lep" Category 2 | 1.75 | 3.13 |
| "Lep" Category 3 | 1.85 | 3.30 |
| "Had" Category 1 | 1.39 | 2.48 |
| "Had" Category 2 | 1.58 | 2.84 |
| "Had" Category 3 | 1.65 | 2.96 |
| "Had" Category 4 | 1.67 | 3.00 |

each category, the specified background-only sample is normalized to agree with the yield of the data sidebands.

Using the specified background-only sample in each category, a signal plus background fit is performed to quantify the potential bias from the choice of analytical function. The fit is performed with fixed Higgs mass values between 121 and 128 GeV with 1 GeV intervals. The maximum of the absolute value of fitted signal yields across the mass range is then defined as the spurious signal systematic for each category. In order for an analytic function to pass the spurious signal test, the spurious signal value must be either less than 10% of the expected Higgs boson yield or less than 20% of the expected error on the extracted signal yield, which is dominated by the statistical uncertainty on the background. Functions passing the spurious signal test criteria must also agree with the data sidebands sufficiently well that $p(\chi^2) > 0.01$. If both functional choices satisfy the spurious signal test and the $\chi^2$ requirement, then the one with the lower spurious signal value is chosen.

The chosen function for the "Had" categories is a power law, with the exception of the category with the greatest signal purity, where an exponential function is chosen. For the "Lep" categories, the exponential function is chosen for the categories with the highest and lowest signal purities, while a power law is chosen for the intermediate category.

# 7 Systematic Uncertainties

## 7.1 Theoretical Sources of Systematic Uncertainty

Theoretical sources of uncertainty considered in the analysis include uncertainties on: Higgs boson branching ratio into the diphoton decay channel (*BR*); the QCD coupling constant $\alpha_s$; the parton distribution function ($t\bar{t}H$ *PDF*); and the parton showering, underlying event, and hadronization model (*UEPS*); and lack of knowledge of higher-order QCD corrections from perturbative calculations (*QCD*). An additional uncertainty on the rates of gluons splitting to heavy-flavor jets and heavy-flavor jets radiated in Higgs boson events from $ggF$, $VH$, and $VBF$ production (*Heavy Flavor*) is included in the analysis, as well.

The uncertainty of the Higgs boson branching ratio is taken from Refs. [44–48]. The effects of uncertainties on $\alpha_s$ and the PDF are estimated based on the recommendations in Ref. [12]. In order to evaluate the effects of incomplete knowledge of parton showering, hadronization processes, and the underlying event, the $t\bar{t}H$ signal yields and kinematic distributions from two alternative samples with the same generator (MADGRAPH5_aMC@NLO) and different parton showering algorithms (HERWIG++ and PYTHIA8) are compared. The uncertainties on the total cross sections of Higgs boson events based on higher-order QCD effects from the $ggF$, $VH$, and $VBF$, $b\bar{b}H$, $tHq$, and $tHW$ production modes are taken from Ref. [25]. Lastly, the yields of Higgs boson events from the $ggF$, $VH$, and $VBF$ production modes with extra heavy-flavor jets are assigned an additional conservative 100% uncertainty (*Heavy Flavor*), which is correlated between the seven analysis categories.

Uncertainties on the $t\bar{t}H$ cross section and the Higgs boson to diphoton branching ratio are included in the signal strength ($\mu_{t\bar{t}H}$) measurement, as $\mu_{t\bar{t}H}$ is scaled by the SM cross section prediction. However, the $t\bar{t}H$ cross section and the Higgs boson to diphoton branching ratio uncertainties are not included in the $t\bar{t}H$ cross section times branching ratio ($\sigma_{t\bar{t}H} \times B_{\gamma\gamma}$) measurement.

Uncertainties on the inclusive Higgs boson event yield from non-$t\bar{t}H$ processes are included in the $t\bar{t}H$ cross section times branching ratio ($\sigma_{t\bar{t}H} \times B_{\gamma\gamma}$) and the signal strength ($\mu_{t\bar{t}H}$) measurements, as all other Higgs boson production processes are assumed to obey their SM predictions. Both the $\mu_{t\bar{t}H}$ and $\sigma_{t\bar{t}H} \times B_{\gamma\gamma}$ measurements take into account uncertainties which may cause event migration between (or out of) BDT categories. These include missing higher-order QCD effects and UEPS uncertainties.

## 7.2 Experimental Sources of Systematic Uncertainty

The sources of experimental uncertainty in the analysis can be roughly separated into two groups: those which primarily impact the signal acceptance or yield and those which primarily impact the signal mass shape. The systematic uncertainties affecting the signal mass shape are photon energy scale (*PES*) and resolution [68] (*PER*). The experimental error on the Higgs boson mass, assigned as 0.24 GeV based on the Run 1 Higgs boson mass measurement [69], also provides an uncertainty on the location of the signal peak. Dominant systematic uncertainties affecting mainly the signal yield include: the integrated luminosity; the efficiency of the diphoton triggers [7]; and pileup modeling. The uncertainty in the combined 2015–2018 integrated luminosity is 1.7%. It is derived, following a methodology similar to that detailed in Ref. [70], and using the LUCID-2 detector for the baseline luminosity measurements [71], from calibration of the luminosity scale using $x$-$y$ beam-separation scans.

Other systematic uncertainties that have an impact on the signal acceptance are described as follows. Photon-related systematic uncertainties include photon identification efficiency and isolation efficiency uncertainties [55]. Jet related systematic uncertainties include the efficiency of the jet-vertex tagger [72] and the jet energy scale and resolution [73]. In addition, systematic uncertainties arising from the reconstruction and identification efficiency of the $b$-tagging algorithm [74, 75] (*Flavor tagging*) used are included, as well. Both electrons [62, 68] and muons [63] contribute with uncertainties associated to the reconstruction, identification efficiency, isolation efficiency, and their respective energy/momentum scales and resolutions. The uncertainty on $E_\mathrm{T}^\mathrm{miss}$ [76] from charged tracks resulting from objects other than the aforementioned high-$p_\mathrm{T}$ objects is taken into account, as well.

Lastly, the uncertainty on the signal yield related to potential background mis-modeling due to the choice of analytic function is accounted for with the spurious signal, calculated for each analysis category, as

described in Section 6. Since no systematic trends were observed between categories in spurious signal studies, the spurious signal uncertainty is left uncorrelated between the BDT categories.

# 8 Statistical Framework

The statistical procedure used to interpret the data is described in Ref. [77] and follows the methods from Ref. [78]. As discussed above, the data are divided into seven $t\bar{t}H$-enriched BDT categories, each with different signal-to-background ratios. For each category, an extended likelihood function is constructed, using as input the $m_{\gamma\gamma}$ distribution of data events in the range $m_{\gamma\gamma} \in [105, 160]$ GeV, and modeled using the signal and background parameterizations derived for that category. The overall likelihood function is the product of the extended likelihoods of the seven categories. Systematic uncertainties are incorporated into the likelihood function using a set of Gaussian or log-normal constraints on nuisance parameters.

The parameter of interest, $\mu$, is the observed cross section times the branching ratio ($\sigma \times BR$) of the $t\bar{t}H$ ($H \to \gamma\gamma$) process, divided by the predicted SM cross section times the SM branching ratio ($\sigma_{SM} \times BR_{SM}$). The cross section times the branching ratio itself is also a parameter of interest. The test statistic relies on the profile likelihood ratio:

$$\Lambda(\mu) = \frac{\mathcal{L}(\mu, \hat{\hat{\theta}}(\mu))}{\mathcal{L}(\hat{\mu}, \hat{\theta})}$$

where $\mathcal{L}$ is the overall likelihood function, $\theta$ is the vector of all nuisance parameters, $\hat{\mu}$ and $\hat{\theta}$ denote the unconditional maximum likelihood estimate of $\mu$, and $\hat{\hat{\theta}}(\mu)$ denotes the conditional maximum likelihood estimate for the nuisance parameters at a fixed value of $\mu$. Agreement of the measured $\mu$ with the null hypothesis (where $\mu$ is defined as 0) is quantified by a $p$-value calculated from the test statistic $\Lambda(\mu = 0)$, which corresponds to evaluating the profile likelihood ratio for a vanishing $t\bar{t}H(H \to \gamma\gamma)$ cross section. This procedure uses the asymptotic formulae presented in Ref. [77].

# 9 Results

The result of the combined fit to the data is shown projected onto each of the BDT categories in Figures 3 and 4 for the "Had" and "Lep" categories, respectively. Similarly, the predicted and observed event yields for each category are presented in Table 3. Results summed over all seven BDT categories are presented in Figure 5; for illustration purposes, events are weighted by $\ln(1 + S_{90}/B_{90})$, where $S_{90}$ ($B_{90}$) for each BDT bin is the expected signal (background) in the smallest $m_{\gamma\gamma}$ window containing 90% of the expected signal. The combined observed significance is $4.9\sigma$, while the expected significance is $4.2\sigma$. The expected significance is evaluated assuming a SM signal and the values of all the nuisance parameters are taken from the nominal fit to the data. The fitted values of the parameters relating to the photon energy scale and resolution are mildly pulled with respect to their nominal values. The expected significance fixing the aforementioned parameters to their nominal value increases to $4.5\sigma$.

The observed signal strength is

$$\mu_{t\bar{t}H} = 1.38\,^{+0.41}_{-0.36} = 1.38\,^{+0.33}_{-0.31}\,(\text{stat.})\,^{+0.13}_{-0.11}\,(\text{exp.})\,^{+0.22}_{-0.14}\,(\text{theo.}).$$

Statistical, experimental and theoretical uncertainties are determined from the difference (in quadrature) of the uncertainty obtained from the unconditional fit and that obtained when the relevant nuisance parameters are fixed to their best fit values.

The observed cross section times branching ratio $\sigma_{t\bar{t}H} \times B_{\gamma\gamma}$ is measured using the same formalism as above. Here, the likelihood function does not include any nuisance parameters representing theoretical uncertainties on the total $t\bar{t}H(\to \gamma\gamma)$ production cross section or on the $H \to \gamma\gamma$ branching ratio. Uncertainties on the kinematic distributions, which may lead to migration between BDT categories or may change the fraction of $t\bar{t}H$ events passing the fiducial requirements, are included in the likelihood function.

The measured cross section times branching ratio is:

$$\sigma_{t\bar{t}H} \times B_{\gamma\gamma} = 1.59^{+0.43}_{-0.39} \text{ fb} = 1.59^{+0.38}_{-0.36} \text{ (stat.) } ^{+0.15}_{-0.12} \text{ (exp.) } ^{+0.15}_{-0.11} \text{ (theo.) fb.}$$

This is compared to the Standard Model prediction of $t\bar{t}H(\to \gamma\gamma) = 1.15^{+0.09}_{-0.12}$ fb. The breakdown of contributions to the measurement from each group of uncertainties is shown in Table 2.

All results are calculated with the Higgs boson mass fixed to $125.09 \pm 0.24$ GeV, the value measured by the ATLAS and CMS Collaborations [69]. As a cross check, the significance, $\mu$, and $\sigma_{t\bar{t}H} \times B_{\gamma\gamma}$ were remeasured with the Higgs boson mass and the signal resolution allowed to be determined directly from data; the results were found to be compatible with the nominal fit.

Table 2: The contribution of groups of systematic uncertainties to the total error on the observed cross section times branching ratio. This is shown as the uncertainty due to each group of systematic uncertainties ($\Delta\sigma$), as a fraction of the total observed cross section ($\sigma$). For each group of uncertainties, asymmetric errors are assigned. Here $\Delta\sigma_{\text{high}}$ ($\Delta\sigma_{\text{low}}$) shows the effect of systematic variations that increase (decrease) $\sigma$.

| Uncertainty source | $\Delta\sigma_{\text{low}}/\sigma$ [%] | $\Delta\sigma_{\text{high}}/\sigma$ [%] |
|---|---|---|
| Theory uncertainties | 6.6 | 9.7 |
| Underlying Event and Parton Shower (UEPS) | 5.0 | 7.2 |
| Modeling of Heavy Flavor Jets in non-$t\bar{t}H$ Processes | 4.0 | 3.4 |
| Higher-Order QCD Terms (QCD) | 3.3 | 4.7 |
| Parton Distribution Function and $\alpha_S$ Scale (PDF+$\alpha_S$) | 0.3 | 0.5 |
| Non-$t\bar{t}H$ Cross Section and Branching Ratio to $\gamma\gamma$ (BR) | 0.4 | 0.3 |
| Experimental uncertainties | 7.8 | 9.1 |
| Photon Energy Resolution (PER) | 5.5 | 6.2 |
| Photon Energy Scale (PES) | 2.8 | 2.7 |
| Jet/$E_{\text{T}}^{\text{miss}}$ | 2.3 | 2.7 |
| Photon Efficiency | 1.9 | 2.7 |
| Background Modeling | 2.1 | 2.0 |
| Flavor Tagging | 0.9 | 1.1 |
| Leptons | 0.4 | 0.6 |
| Pileup | 1.0 | 1.5 |
| Luminosity and Trigger | 1.6 | 2.3 |
| Higgs Boson Mass | 1.6 | 1.5 |
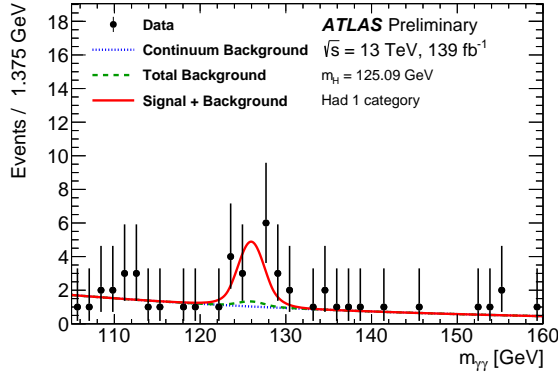
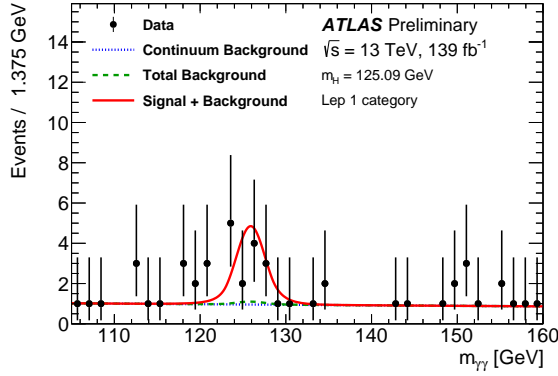(a) "Had" Category 1
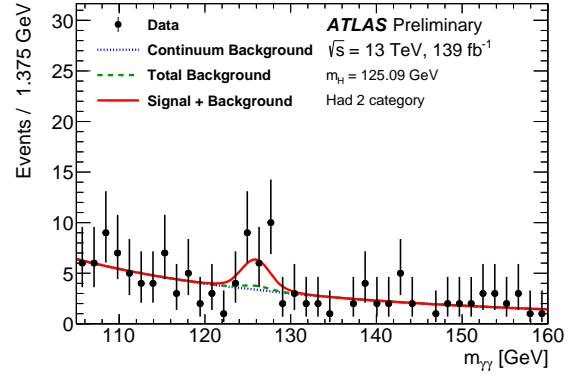


(b) "Had" Category 2
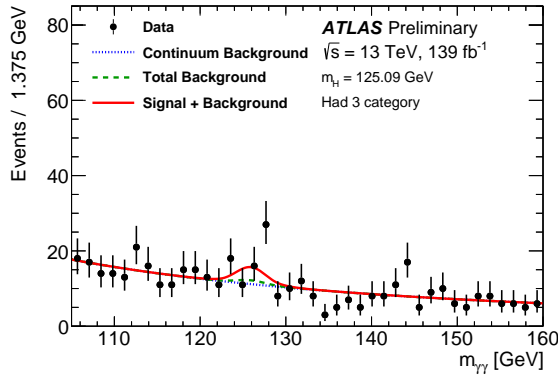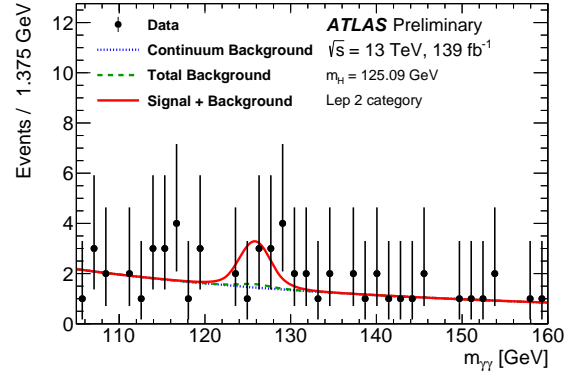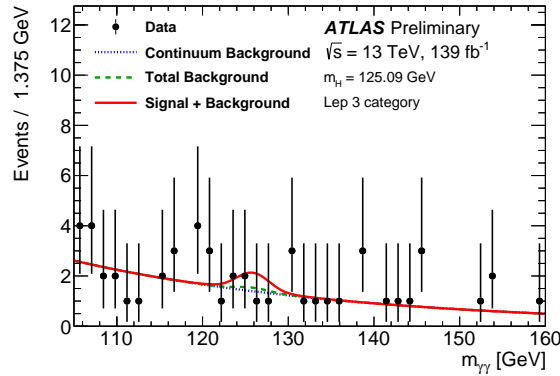


(c) "Had" Category 3
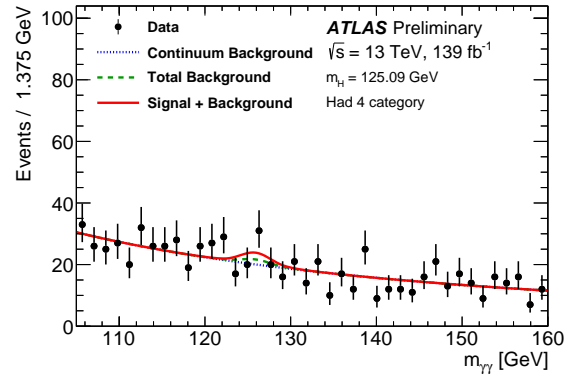


(d) "Had" Category 4

Figure 3: The fitted signal and background shapes for each of the four "Had" region BDT categories. The category with the greatest purity is shown in (a), the second-greatest purity in (b), the third-greatest purity in (c), and the lowest purity in (d). The red line shows the result of the signal plus background unbinned fit to the data, while the data points are shown as black dots. The dotted blue line shows the continuum background component of the fit, and the dashed green line shows the total background (including non-$t\bar{t}H$ Higgs events). The fit results are derived from the combined signal plus background fit to all seven BDT categories.

(a) "Lep" Category 1



(b) "Lep" Category 2



(c) "Lep" Category 3

Figure 4: The fitted signal and background shapes for each of the three "Lep" region BDT categories, with (a) showing the category with the greatest signal purity and (c) showing that with the lowest. The category with intermediate purity is shown in (b). The red line shows the result of the signal plus background unbinned fit to the data, while the data points are shown as black dots. The dotted blue line shows the continuum background component of the fit, and the dashed green line shows the total background (including non-$t\bar{t}H$ Higgs events). The fit results are derived from the combined signal plus background fit to all seven BDT categories.
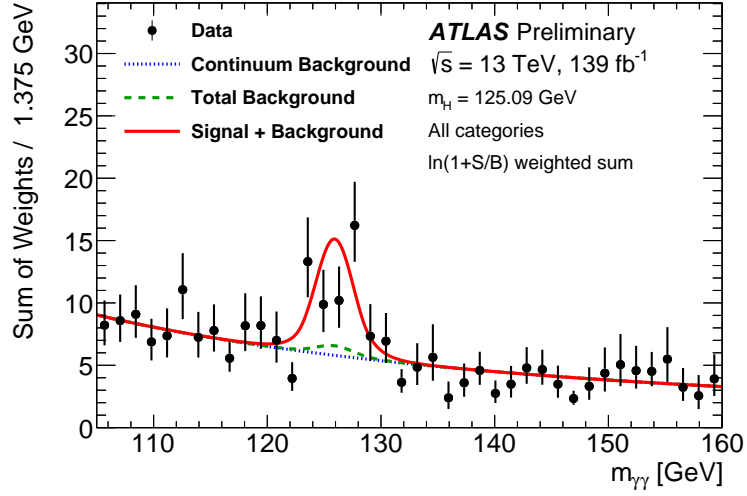
Figure 5: Weighted diphoton invariant mass spectrum for the sum of all BDT categories observed in 139 fb$^{-1}$ of 13 TeV data. Events are weighted by $\ln(1 + S_{90}/B_{90})$, where $S_{90}$ ($B_{90}$) for each BDT category is the expected signal (background) in the smallest $m_{\gamma\gamma}$ window containing 90% of the expected signal. The error bars represent 68% confidence intervals of the weighted sums. The solid red curve shows the fitted signal-plus-background model with the Higgs boson mass constrained to $125.09 \pm 0.24$ GeV. The non-resonant and total background components of the fit are shown with the dotted blue curve and dashed green curve. Both the signal-plus-background and background-only curves shown here are obtained from the weighted sum of the individual curves in each BDT category.

Table 3: Observed number of events in the different categories for the cross section times branching ratio measurement, using 13 TeV data corresponding to an integrated luminosity of 139 fb$^{-1}$ ("Data"). The observed yields are compared with the sum of expected $t\bar{t}H$ signal, background from non-$t\bar{t}H$ Higgs boson production, and other background sources. The numbers are counted in the smallest $m_{\gamma\gamma}$ window containing 90% of the expected signal. The background yield is extracted from the fit with freely floating signal. The BDT bins are labeled such that the category with the highest signal purity in each of the "Had" and "Lep" regions is labeled as category 1, while that with the lowest signal purity is labeled with the largest number.

| Category | $t\bar{t}H$ Signal | non-$t\bar{t}H$ Higgs | Continuum Background | Total (Expected) | Data |
|---|---|---|---|---|---|
| $t\bar{t}H$ "Lep" Category 1 | $7.9 \pm 1.5$ | $0.42 \pm 0.12$ | $4.6 \pm 0.9$ | $12.9 \pm 1.8$ | 15 |
| $t\bar{t}H$ "Lep" Category 2 | $3.9 \pm 0.6$ | $0.43 \pm 0.15$ | $7.5 \pm 1.2$ | $11.8 \pm 1.3$ | 11 |
| $t\bar{t}H$ "Lep" Category 3 | $1.45 \pm 0.24$ | $0.49 \pm 0.19$ | $7.5 \pm 1.2$ | $9.5 \pm 1.2$ | 6 |
| $t\bar{t}H$ "Had" Category 1 | $6.9 \pm 1.6$ | $0.8 \pm 0.5$ | $4.5 \pm 0.9$ | $12.2 \pm 1.9$ | 15 |
| $t\bar{t}H$ "Had" Category 2 | $5.6 \pm 1.0$ | $1.1 \pm 0.8$ | $16.5 \pm 1.7$ | $23.2 \pm 2.3$ | 31 |
| $t\bar{t}H$ "Had" Category 3 | $7.7 \pm 1.3$ | $3.1 \pm 2.2$ | $56.0 \pm 3.0$ | $67 \pm 4$ | 82 |
| $t\bar{t}H$ "Had" Category 4 | $4.9 \pm 0.8$ | $5 \pm 4$ | $101 \pm 4$ | $111 \pm 6$ | 105 |

15

# 10 Conclusion

A measurement of Higgs boson production in association with a top quark-antiquark pair ($t\bar{t}H$) in the diphoton decay mode has been presented. The dataset used corresponds to 139 fb$^{-1}$ of proton–proton collision data at a center-of-mass energy of 13 TeV, produced by the Large Hadron Collider and recorded with the ATLAS detector. The $t\bar{t}H$ process is observed in the diphoton decay mode with a significance of 4.9 standard deviations relative to the background-only hypothesis. The expected significance is 4.2 standard deviations. The $t\bar{t}H$ cross-section times the $H \rightarrow \gamma\gamma$ branching ratio is measured to be $\sigma_{t\bar{t}H} \times B_{\gamma\gamma} = 1.59^{+0.43}_{-0.39}$ fb, in agreement with the Standard Model prediction of $t\bar{t}H(\rightarrow \gamma\gamma) = 1.15^{+0.09}_{-0.12}$ fb.
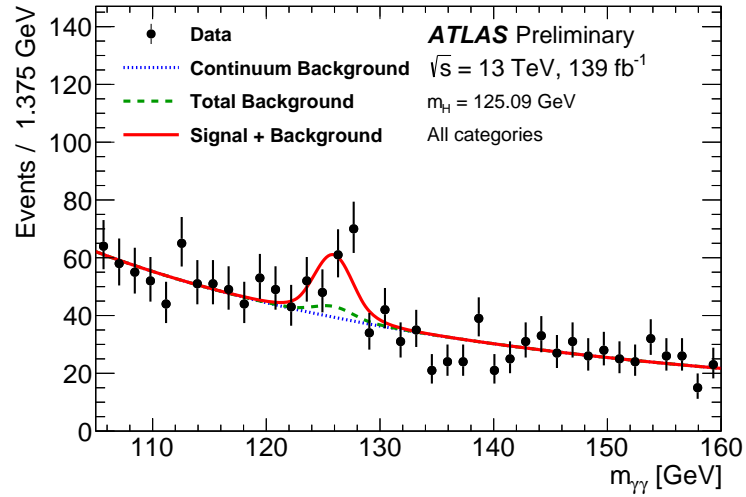
# Appendix



Figure 6: Unweighted diphoton invariant mass spectrum for the sum of all BDT categories observed in 140 fb$^{-1}$ of 13 TeV data. The solid red curve shows the fitted signal-plus-background model with the Higgs boson mass constrained to 125.09 ± 0.24 GeV. The non-resonant and total background components of the fit are shown with the dotted blue curve and dashed green curve. Both the signal-plus-background and background-only curves shown here are obtained from the sum of the individual curves in each BDT category.
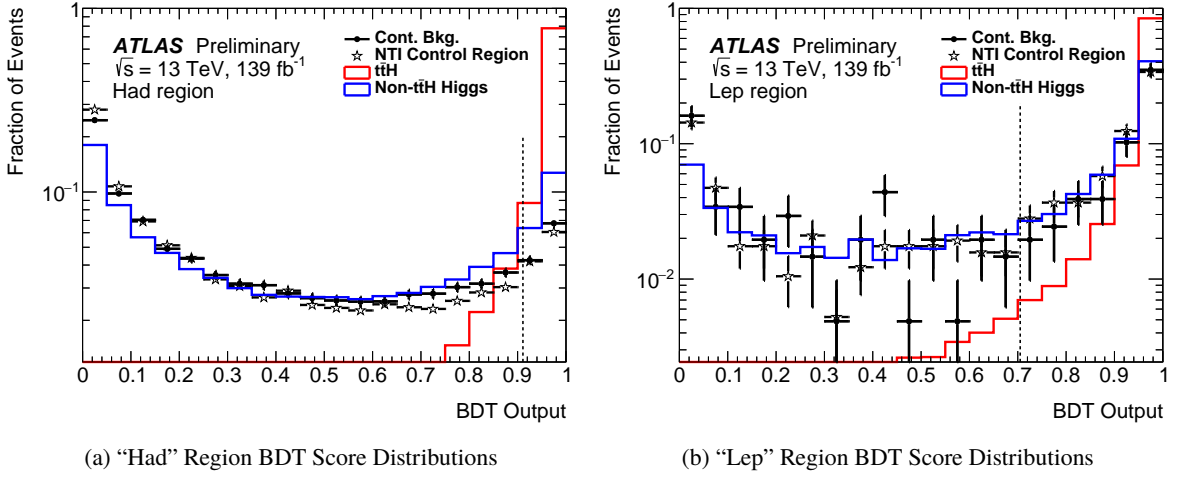
(a) "Had" Region BDT Score Distributions

(b) "Lep" Region BDT Score Distributions

Figure 7: The normalized fraction of events in bins of BDT score in the (a) "Had" and (b) "Lep" regions of: simulated $t\bar{t}H$ signal events (red); simulated non-$t\bar{t}H$ Higgs boson events (blue); "Not Tight/Isolated" data events used as the background sample in testing the BDTs (open stars); and data sideband events (filled black circles). The "Not Tight/Isolated" (NTI) data events shown are those used in testing the BDTs, and, as such, they are required to pass all cuts in the diphoton and $t\bar{t}H$ preselections, other than the identification and isolation criteria. The dashed line denotes the BDT-score cut of the loosest category in each region.
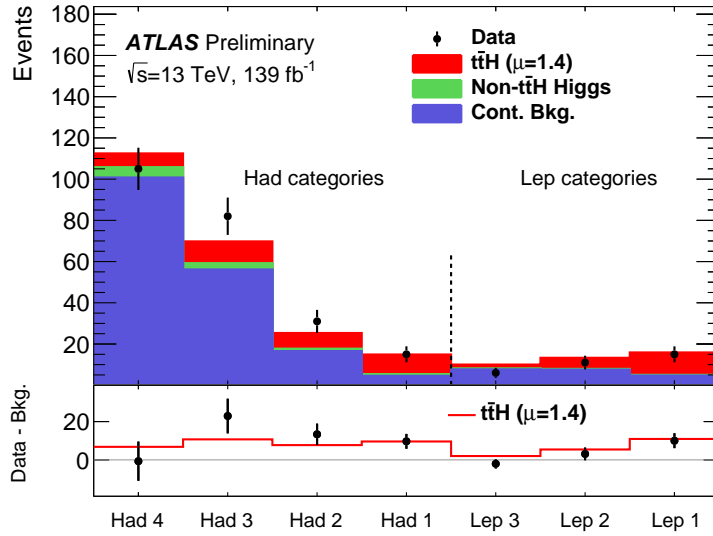


Figure 8: The number of data events in the different analysis BDT bins, in the smallest diphoton mass window that contains 90% of the $t\bar{t}H$ signal, shown with black points. The expected continuum background is extracted from the diphoton mass fits in each category and is shown in purple. The non-$t\bar{t}H$ Higgs boson background is shown in green, and the $t\bar{t}H$ signal (for a signal strength $\mu = \sigma/\sigma_{SM}$ of 1.4) is shown in red. The lower panel shows the residuals between the data and the background in black points, as well as the predicted $t\bar{t}H$ signal with $\mu = 1.4$ as the red line.
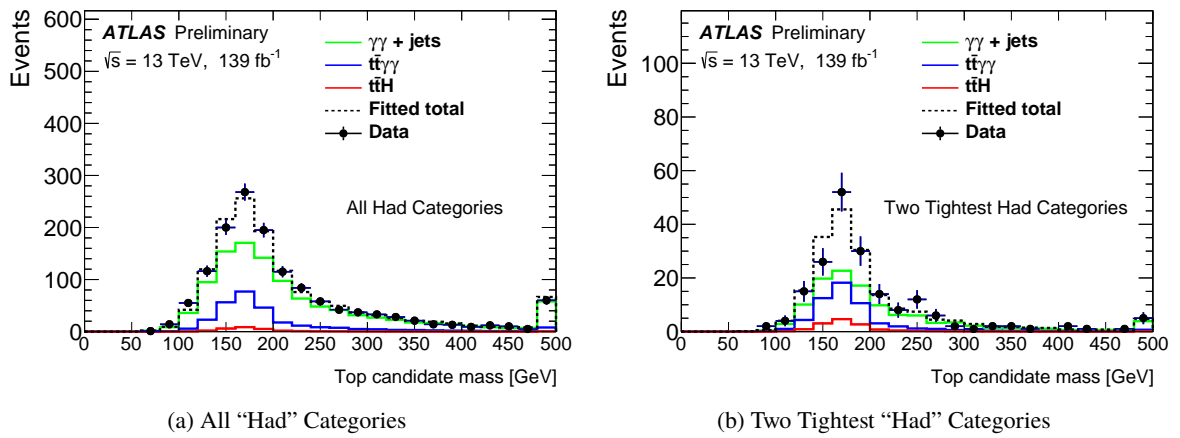
(a) All "Had" Categories      (b) Two Tightest "Had" Categories

Figure 9: The reconstructed top mass obtained using a dedicated top-reconstruction BDT for (a) all "Had" region categories and (b) the two tightest "Had" region categories. The green line shows the distribution of simulated continuum diphoton events, the blue line shows the distribution of simulated $t\bar{t}\gamma\gamma$ events, and the red line shows the distribution of simulated $t\bar{t}H$ signal events. The magnitude of the $t\bar{t}H$ signal is fixed to the standard model expectation. The magnitudes of the background components are determined by performing a template fit to the data distribution, shown by the black points. The total fitted distribution is shown by the dashed black line and shows good agreement with the data points in both cases. The results of the template fit predict that the four "Had" categories contain approximately $21 \pm 6\%$ $t\bar{t}\gamma\gamma$ events, while the tightest two categories contain approximately $31 \pm 17\%$ $t\bar{t}\gamma\gamma$ events. Although the uncertainties are large, the significant fraction of predicted $t\bar{t}\gamma\gamma$ events suggests that the "Had" BDT does select for events which are consistent with containing a top quark.

# References

[1] ATLAS Collaboration, *Observation of a new particle in the search for the Standard Model Higgs boson with the ATLAS detector at the LHC*, Phys. Lett. B **716** (2012) 1, arXiv: 1207.7214 [hep-ex].

[2] CMS Collaboration, *Observation of a new boson at a mass of 125 GeV with the CMS experiment at the LHC*, Phys. Lett. B **716** (2012) 30, arXiv: 1207.7235 [hep-ex].

[3] ATLAS Collaboration, *Observation of Higgs boson production in association with a top quark pair at the LHC with the ATLAS detector*, Phys. Lett. B **784** (2018) 173, arXiv: 1806.00425 [hep-ex].

[4] CMS Collaboration, *Observation of tt̄H Production*, Phys. Rev. Lett. **120** (2018) 231801, arXiv: 1804.02610 [hep-ex].

[5] ATLAS Collaboration, *The ATLAS Experiment at the CERN Large Hadron Collider*, JINST **3** (2008) S08003.

[6] ATLAS Collaboration, *ATLAS Insertable B-Layer Technical Design Report*, ATLAS-TDR-19, 2010, URL: https://cds.cern.ch/record/1291633,
*ATLAS Insertable B-Layer Technical Design Report Addendum*, ATLAS-TDR-19-ADD-1, 2012, URL: https://cds.cern.ch/record/1451888.

[7] ATLAS Collaboration, *Performance of the ATLAS trigger system in 2015*, Eur. Phys. J. C **77** (2017) 317, arXiv: 1611.09661 [hep-ex].

[8] P. Nason, *A New method for combining NLO QCD with shower Monte Carlo algorithms*, JHEP **11** (2004) 040, arXiv: hep-ph/0409146.

[9] S. Frixione, P. Nason and C. Oleari, *Matching NLO QCD computations with parton shower simulations: the POWHEG method*, JHEP **11** (2007) 070, arXiv: 0709.2092 [hep-ph].

[10] S. Alioli, P. Nason, C. Oleari and E. Re, *A general framework for implementing NLO calculations in shower Monte Carlo programs: the POWHEG BOX*, JHEP **06** (2010) 043, arXiv: 1002.2581 [hep-ph].

[11] J. M. Campbell et al., *NLO Higgs boson production plus one and two jets using the POWHEG BOX, MadGraph4 and MCFM*, JHEP **07** (2012) 092, arXiv: 1202.5475 [hep-ph].

[12] J. Butterworth et al., *PDF4LHC recommendations for LHC Run II*, J. Phys. G **43** (2016) 023001, arXiv: 1510.03865 [hep-ph].

[13] T. Sjöstrand, S. Mrenna and P. Z. Skands, *A brief introduction to PYTHIA 8.1*, Comput. Phys. Commun. **178** (2008) 852, arXiv: 0710.3820 [hep-ph].

[14] ATLAS Collaboration, *ATLAS Pythia 8 tunes to 7 TeV data*, ATL-PHYS-PUB-2014-021, 2014, URL: https://cds.cern.ch/record/1966419.

[15] K. Hamilton, P. Nason, E. Re and G. Zanderighi, *NNLOPS simulation of Higgs boson production*, JHEP **10** (2013) 222, arXiv: 1309.0017 [hep-ph].

[16] P. Nason and C. Oleari, *NLO Higgs boson production via vector-boson fusion matched with shower in POWHEG*, JHEP **02** (2010) 037, arXiv: 0911.5299 [hep-ph].

[17] K. Mimasu, V. Sanz and C. Williams, *Higher order QCD predictions for associated Higgs production with anomalous couplings to gauge bosons*, JHEP **08** (2016) 039, arXiv: 1512.02572 [hep-ph].

[18] G. Luisoni, P. Nason, C. Oleari and F. Tramontano, *HW$^{\pm}$/HZ + 0 and 1 jet at NLO with the POWHEG BOX interfaced to GoSam and their merging within MiNLO*, JHEP **10** (2013) 083, arXiv: 1306.2542 [hep-ph].

[19] ATLAS Collaboration, *Measurement of the $Z/\gamma^*$ boson transverse momentum distribution in pp collisions at $\sqrt{s}$ = 7 TeV with the ATLAS detector*, JHEP **09** (2014) 145, arXiv: 1406.3660 [hep-ex].

[20] J. Alwall et al., *The automated computation of tree-level and next-to-leading order differential cross sections, and their matching to parton shower simulations*, JHEP **07** (2014) 079, arXiv: 1405.0301 [hep-ph].

[21] H.-L. Lai et al., *New parton distributions for collider physics*, Phys. Rev. D **82** (2010) 074024, arXiv: 1007.2241 [hep-ph].

[22] S. Gieseke, A. Ribon, M. H. Seymour, P. Stephens and B. Webber, *Herwig++ 1.0: an event generator for $e^+ e^-$ annihilation*, JHEP **02** (2004) 005, arXiv: hep-ph/0311208.

[23] J. Bellm et al., *Herwig++ 2.7 Release Note*, 2013, arXiv: 1310.6877 [hep-ph].

[24] M. Bahr et al., *Herwig++ physics and manual*, Eur. Phys. J. C **58** (2008) 639, arXiv: 0803.0883 [hep-ph].

[25] LHC Higgs Cross Section Working Group (D. de Florian et al.), *Handbook of LHC Higgs Cross Sections: 4. Deciphering the Nature of the Higgs Sector*, 2016, arXiv: 1610.07922 [hep-ph].

[26] C. Anastasiou, C. Duhr, F. Dulat, F. Herzog and B. Mistlberger, *Higgs Boson Gluon-Fusion Production in QCD at Three Loops*, Phys. Rev. Lett. **114** (2015) 212001, arXiv: 1503.06056 [hep-ph].

[27] C. Anastasiou et al., *High precision determination of the gluon fusion Higgs boson cross-section at the LHC*, JHEP **05** (2016) 058, arXiv: 1602.00695 [hep-ph].

[28] S. Actis, G. Passarino, C. Sturm and S. Uccirati, *NLO electroweak corrections to Higgs boson production at hadron colliders*, Phys. Lett. B **670** (2008) 12, arXiv: 0809.1301 [hep-ph].

[29] C. Anastasiou, R. Boughezal and F. Petriello, *Mixed QCD-electroweak corrections to Higgs boson production in gluon fusion*, JHEP **04** (2009) 003, arXiv: 0811.3458 [hep-ph].

[30] M. Ciccolini, A. Denner and S. Dittmaier, *Strong and electroweak corrections to the production of Higgs + 2 jets via weak interactions at the LHC*, Phys. Rev. Lett. **99** (2007) 161803, arXiv: 0707.0381 [hep-ph].

[31] M. Ciccolini, A. Denner and S. Dittmaier, *Electroweak and QCD corrections to Higgs production via vector-boson fusion at the LHC*, Phys. Rev. D **77** (2008) 013002, arXiv: 0710.4749 [hep-ph].

[32] P. Bolzoni, F. Maltoni, S.-O. Moch and M. Zaro,
*Higgs production via vector-boson fusion at NNLO in QCD*, Phys. Rev. Lett. **105** (2010) 011801,
arXiv: 1003.4451 [hep-ph].

[33] O. Brein, A. Djouadi and R. Harlander,
*NNLO QCD corrections to the Higgs-strahlung processes at hadron colliders*,
Phys. Lett. B **579** (2004) 149, arXiv: hep-ph/0307206.

[34] L. Altenkamp, S. Dittmaier, R. V. Harlander, H. Rzehak and T. J. E. Zirke,
*Gluon-induced Higgs-strahlung at next-to-leading order QCD*, JHEP **02** (2013) 078,
arXiv: 1211.5015 [hep-ph].

[35] A. Denner, S. Dittmaier, S. Kallweit and A. Mück, *Electroweak corrections to Higgs-strahlung off
W/Z bosons at the Tevatron and the LHC with HAWK*, JHEP **03** (2012) 075,
arXiv: 1112.5142 [hep-ph].

[36] W. Beenakker et al., *NLO QCD corrections to $t\bar{t}H$ production in hadron collisions*,
Nucl. Phys. B **653** (2003) 151, arXiv: hep-ph/0211352.

[37] S. Dawson, C. Jackson, L. Orr, L. Reina and D. Wackeroth,
*Associated Higgs production with top quarks at the large hadron collider: NLO QCD corrections*,
Phys. Rev. D **68** (2003) 034022, arXiv: hep-ph/0305087.

[38] Y. Zhang, W.-G. Ma, R.-Y. Zhang, C. Chen and L. Guo,
*QCD NLO and EW NLO corrections to $t\bar{t}H$ production with top quark decays at hadron collider*,
Phys. Lett. B **738** (2014) 1, arXiv: 1407.1110 [hep-ph].

[39] S. Frixione, V. Hirschi, D. Pagani, H.-S. Shao and M. Zaro,
*Electroweak and QCD corrections to top-pair hadroproduction in association with heavy bosons*,
JHEP **06** (2015) 184, arXiv: 1504.03446 [hep-ph].

[40] S. Dawson, C. Jackson, L. Reina and D. Wackeroth,
*Exclusive Higgs boson production with bottom quarks at hadron colliders*,
Phys. Rev. D **69** (2004) 074027, arXiv: hep-ph/0311067.

[41] S. Dittmaier, M. Krämer and M. Spira,
*Higgs radiation off bottom quarks at the Tevatron and the CERN LHC*,
Phys. Rev. D **70** (2004) 074010, arXiv: hep-ph/0309204.

[42] R. Harlander, M. Kramer and M. Schumacher, *Bottom-quark associated Higgs-boson production:
reconciling the four- and five-flavour scheme approach*, 2011, arXiv: 1112.3478 [hep-ph].

[43] F. Demartin, F. Maltoni, K. Mawatari and M. Zaro,
*Higgs production in association with a single top quark at the LHC*, Eur. Phys. J. C **75** (2015) 267,
arXiv: 1504.00611 [hep-ph].

[44] A. Djouadi, J. Kalinowski and M. Spira, *HDECAY: a program for Higgs boson decays in the
Standard Model and its supersymmetric extension*, Comput. Phys. Commun. **108** (1998) 56,
arXiv: hep-ph/9704448.

[45] A. Djouadi, M. M. Mühlleitner and M. Spira,
*Decays of supersymmetric particles: The Program SUSY-HIT (SUspect-SdecaY-Hdecay-InTerface)*,
Acta Phys. Polon. **B38** (2007) 635, arXiv: hep-ph/0609292.

[46] A. Bredenstein, A. Denner, S. Dittmaier and M. M. Weber, *Radiative corrections to the
semileptonic and hadronic Higgs-boson decays $H \to WW/ZZ \to 4$ fermions*, JHEP **02** (2007) 080,
arXiv: hep-ph/0611234.

[47] A. Bredenstein, A. Denner, S. Dittmaier and M. M. Weber,
*Precise predictions for the Higgs-boson decay H → WW/ZZ → 4 leptons*,
Phys. Rev. D **74** (2006) 013004, arXiv: hep-ph/0604011.

[48] A. Bredenstein, A. Denner, S. Dittmaier and M. M. Weber,
*Precision calculations for the Higgs decays H → ZZ/WW → 4 leptons*,
Nucl. Phys. Proc. Suppl. **160** (2006) 131, arXiv: hep-ph/0607060.

[49] T. Gleisberg et al., *Event generation with SHERPA 1.1*, JHEP **02** (2009) 007,
arXiv: 0811.4622 [hep-ph].

[50] S. Höche, F. Krauss, M. Schonherr and F. Siegert,
*QCD matrix elements + parton showers: The NLO case*, JHEP **04** (2013) 027,
arXiv: 1207.5030 [hep-ph].

[51] GEANT4 Collaboration, *GEANT4: a simulation toolkit*, Nucl. Instrum. Meth. A **506** (2003) 250.

[52] ATLAS Collaboration, *The ATLAS Simulation Infrastructure*, Eur. Phys. J. C **70** (2010) 823,
arXiv: 1005.4568 [physics.ins-det].

[53] ATLAS Collaboration,
*The simulation principle and performance of the ATLAS fast calorimeter simulation FastCaloSim*,
ATL-PHYS-PUB-2010-013, 2010, URL: https://cds.cern.ch/record/1300517.

[54] ATLAS Collaboration,
*Topological cell clustering in the ATLAS calorimeters and its performance in LHC Run 1*,
Eur. Phys. J. C **77** (2017) 490, arXiv: 1603.02934 [hep-ex].

[55] ATLAS Collaboration, *Measurement of the photon identification efficiencies with the ATLAS
detector using LHC Run 2 data collected in 2015 and 2016*, Accepted to: Eur. Phys. J. (2018),
arXiv: 1810.05087 [hep-ex].

[56] ATLAS Collaboration, *Electron and photon reconstruction and performance in ATLAS using a
dynamical, topological cell clustering-based approach*, ATL-PHYS-PUB-2017-022, 2017,
URL: https://cds.cern.ch/record/2298955.

[57] ATLAS Collaboration, *Measurement of Higgs boson production in the diphoton decay channel in
pp collisions at center-of-mass energies of 7 and 8 TeV with the ATLAS detector*,
Phys. Rev. D **90** (2014) 112015, arXiv: 1408.7084 [hep-ex].

[58] M. Cacciari, G. P. Salam and G. Soyez, *The anti-$k_t$ jet clustering algorithm*, JHEP **04** (2008) 063,
arXiv: 0802.1189 [hep-ph].

[59] ATLAS Collaboration, *Expected performance of the ATLAS b-tagging algorithms in Run-2*,
ATL-PHYS-PUB-2015-022, 2015, URL: https://cds.cern.ch/record/2037697.

[60] ATLAS Collaboration,
*Measurements of b-jet tagging efficiency with the ATLAS detector using $t\bar{t}$ events at $\sqrt{s}$ = 13 TeV*,
JHEP **08** (2018) 089, arXiv: 1805.01845 [hep-ex].

[61] ATLAS Collaboration, *Performance of pile-up mitigation techniques for jets in pp collisions at
$\sqrt{s}$ = 8 TeV using the ATLAS detector*, Eur. Phys. J. C **76** (2016) 581,
arXiv: 1510.03823 [hep-ex].

[62] ATLAS Collaboration, *Electron reconstruction and identification in the ATLAS experiment using
the 2015 and 2016 LHC proton-proton collision data at $\sqrt{s}$ = 13 TeV*,
Submitted to: Eur. Phys. J. (2019), arXiv: 1902.04655 [physics.ins-det].

[63] ATLAS Collaboration, *Muon reconstruction performance of the ATLAS detector in proton–proton collision data at* $\sqrt{s}$ = 13 *TeV*, Eur. Phys. J. C **76** (2016) 292, arXiv: 1603.05598 [hep-ex].

[64] ATLAS Collaboration, *Performance of missing transverse momentum reconstruction with the ATLAS detector using proton–proton collisions at* $\sqrt{s}$ = 13 *TeV*, Eur. Phys. J. C **78** (2018) 903, arXiv: 1802.08168 [hep-ex].

[65] T. Chen and C. Guestrin, *XGBoost: A Scalable Tree Boosting System*, arXiv: 1603.02754 [cs.LG].

[66] M. Oreglia, 'A Study of the Reactions $\psi' \rightarrow \gamma\gamma\psi$', PhD thesis: SLAC, 1980, URL: http://www-public.slac.stanford.edu/sciDoc/docMeta.aspx?slacPubNumber=slac-r-236.html.

[67] ATLAS Collaboration, *Search for Scalar Diphoton Resonances in the Mass Range 65–600 GeV with the ATLAS Detector in pp Collision Data at* $\sqrt{s}$ = 8 *TeV*, Phys. Rev. Lett. **113** (17 2014) 171801, URL: https://link.aps.org/doi/10.1103/PhysRevLett.113.171801.

[68] ATLAS Collaboration, *Electron and photon energy calibration with the ATLAS detector using 2015-2016 LHC proton-proton collision data*, Submitted to: JINST (2018), arXiv: 1812.03848 [hep-ex].

[69] ATLAS and CMS Collaborations, *Combined Measurement of the Higgs Boson Mass in pp Collisions at* $\sqrt{s}$ = 7 *and* 8 *TeV with the ATLAS and CMS Experiments*, Phys. Rev. Lett. **114** (2015) 191803, arXiv: 1503.07589 [hep-ex].

[70] ATLAS Collaboration, *Luminosity determination in pp collisions at* $\sqrt{s}$ = 8 *TeV using the ATLAS detector at the LHC*, Eur. Phys. J. C **76** (2016) 653, arXiv: 1608.03953 [hep-ex].

[71] G. Avoni et al., *The new LUCID-2 detector for luminosity measurement and monitoring in ATLAS*, JINST **13** (2018) P07017.

[72] ATLAS Collaboration, *Vertex Reconstruction Performance of the ATLAS Detector at* $\sqrt{s}$ = 13 *TeV*, ATL-PHYS-PUB-2015-026, 2015, URL: https://cds.cern.ch/record/2037717.

[73] ATLAS Collaboration, *Jet energy scale measurements and their systematic uncertainties in proton–proton collisions at* $\sqrt{s}$ = 13 *TeV with the ATLAS detector*, Phys. Rev. D **96** (2017) 072002, arXiv: 1703.09665 [hep-ex].

[74] ATLAS Collaboration, *Performance of b-jet identification in the ATLAS experiment*, JINST **11** (2016) P04008, arXiv: 1512.01094 [hep-ex].

[75] ATLAS Collaboration, *Measurement of b-tagging efficiency of c-jets in* $t\bar{t}$ *events using a likelihood approach with the ATLAS detector*, ATLAS-CONF-2018-001, 2018, URL: https://cds.cern.ch/record/2306649.

[76] ATLAS Collaboration, $E_T^{miss}$ *performance in the ATLAS detector using 2015–2016 LHC pp collisions*, ATLAS-CONF-2018-023, 2018, URL: https://cds.cern.ch/record/2625233.

[77] "ATLAS and C. Collaborations", *Procedure for the LHC Higgs boson search combination in Summer 2011*, tech. rep. CMS-NOTE-2011-005. ATL-PHYS-PUB-2011-11, CERN, 2011, URL: https://cds.cern.ch/record/1379837.

[78] ATLAS Collaboration, *Measurements of Higgs boson properties in the diphoton decay channel with 36 fb$^{-1}$ of pp collision data at $\sqrt{s}$ = 13 TeV with the ATLAS detector*, Phys. Rev. **D98** (2018) 052005, arXiv: 1802.04146 [hep-ex].